Fully integrated point-of-care blood cell count using multi-frame morphology analysis

Wenchang Zhang [a,*,1], Ya Li [b,1], Bing Chen [b,1], Yuan Zhang [c], Ziqiang Du [d], Feibin Xiang [a], Yu Hu [d], Xiaochen Meng [e], Chunliang Shang [f], Shengfa Liang [a], Xiaonan Yang [d,**], Weihua Guan [g,h,***]

[a] Key Lab of Microelectronic Devices & Integrated Technology, Institute of Microelectronics, Chinese Academy of Sciences, Beijing, 100029, China
[b] Department of Gastroenterology, The First Affiliated Hospital of Zhengzhou University, Zhengzhou, 450052, China
[c] Key Clinical Laboratory of Henan Province, Department of Clinical Laboratory, The First Affiliated Hospital of Zhengzhou University, Zhengzhou, 450052, China
[d] School of Information Engineering, Zhengzhou University, Zhengzhou, 450001, China
[e] Key Laboratory of the Ministry of Education for Optoelectronic Measurement Technology and Instrument, Beijing Information Science & Technology University, Beijing, 100192, China
[f] Department of Obstetrics and Gynecology, Peking University Third Hospital, Beijing, 100191, China
[g] Department of Electrical Engineering, Pennsylvania State University, University Park, 16802, USA
[h] Department of Biomedical Engineering, Pennsylvania State University, University Park, 16802, USA

ARTICLE INFO

ABSTRACT

Point-of-care testing (POCT) of blood cell count (BCC) is an emerging approach that allows laypersons to identify and count whole blood cells through simple manipulation. To date, POCTs for BCC were mainly achieved by "stationary" images through blood smears or single-laity arranged cells in the microwell, making it difficult to obtain statistically sufficient numbers of cells. In this work, we present a fully integrated POCT device solely using "in-flow" imaging of 3 μL fingertip whole blood for improved identification and counting accuracy of BCC analysis. A miniaturized magnetic stirring module was integrated to maintain the temporal stability of cell concentration. A relatively high throughput (~8000 cells/min) with a 30-fold dilution ratio of whole blood can be tested for as long as 1 h to examine sufficient numbers of cells, and the subclass cell concentration keeps constant. To improve the identification accuracy, multi-frame "in-flow" imaging was used to track the cell motion trails with multi-angle morphology analysis. This proof-of-concept was then validated with healthy whole blood samples and 75 cases of clinical patients with abnormal concentrations of red blood cells (RBCs), white blood cells (WBCs), and platelets (PLT). The average precision (AP) value of WBCs identification was improved from 0.8622 to 0.9934 using the multi-frame analysis method. And the high fitting degrees (>0.98) between our POCT device and the commercial clinical equipment indicated good agreement. This POCT device is user-friendly and cost-effective, making it a potential tool for diagnosing abnormal blood cell morphology or concentration in the field setting.

1. Introduction

The quantity of human blood cells, including the counts of red blood cells (RBCs), white blood cells (WBCs), and platelets (PLTs) has been proven to play important roles in the revelation of various biological activities and can serve as promising markers of physiological states (Beck, 2009). However, most commonly used clinical detection methods depend on elaborate equipment and professional operations, which are not available for some cases like bedside or physician's office testing (Yang et al., 2019). The point-of-care testing (POCT) is now common in many near-patient and critical care settings. POCT method and system of blood cell count (BCC), including subpopulation recognition and

counting, is of great significance and strong demand for low-cost, rapid detection, and health monitoring in both resource-limited areas and developed countries.

Owing to the unique advantages of microfluidic technology in sample utilization, cell analysis, and manipulation, as well as the great potential in system miniaturization and integration, a lot of useful research on POCT for BCC based on the microfluidic method has been carried out in the past decades. For example, according to the physical or chemical character difference of blood cells, various methods based on electrical impedance (Wang et al., 2022; Zhang et al., 2019), specificity-based capture (Kanakasabapathy et al., 2017), fluorescence staining (Zhu et al., 2011), and microscopy imaging (Hernandez-Neuta et al., 2019; Ilyas et al., 2020; Kheireddine et al., 2019; Merazzo et al., 2021) were integrated onto microfluidic chips for BCC. Among them, the microscopic imaging method stands out due to its capability of visualization of morphology and thus enhanced specificity (Yang et al., 2019). In particular, the widespread popularity of miniaturized high-performance imaging devices (smartphones, webcams. etc.) and the development of deep learning methods (Balsam et al., 2014; Wu et al., 2013; Zare Harofte et al., 2022; Zhu et al., 2013) have tremendously expanded the application potential. To facilitate the whole device integration, a lot of efforts have been made to miniaturize the microscope system for either single-lens or multiple-lens (Skandarajah et al., 2014), for example, the field of view (FOV), spatial resolution, and image contrast (Meng et al., 2016) were analyzed using different lens types (Smith et al., 2011), focal length, numerical aperture (NA), image sensor performance (Skandarajah et al., 2014), illumination patterns (Kanakasabapathy et al., 2019; Orth et al., 2018), and combined with distortions correction methods (Rivenson et al., 2018). Current studies are mostly using high-quality morphological images of stationary cells (such as peripheral blood smears), as well as the cells set in a fixed imaging region of the microfluidic chip, and realized a variety of applications, including the analysis of stained and unstained blood smears, cell migration, sickle cell disease (Ilyas et al., 2020), megaloblastic anemia, myelofibrosis, thrombotic thrombocytopenic purpura, thalassemia (Chen et al., 2021), natural killer cells quantification and subpopulation (Ryan Zenhausern, 2022). Etc. However, due to the tradeoff between spatial resolution and FOV, these "stationary imaging" methods can hardly get a statistically sufficient number of measured cells for BCC (Go et al., 2018).

To improve the statistical analysis accuracy, two major directions are explored to increase the number of measured cells: enlarging the imaging area and "in-flow" imaging. An ultra-wide FOV could be achieved with lensless/lens-free imaging (Go et al., 2018; Lee and Yang, 2014; Roy et al., 2017) or by mounting the microscope on a motorized stage for scanning microscopy (Walzik et al., 2015) of a large number of cells. However, the complexity of lensless imaging reconstruction algorithms, as well as the ultra-high positioning accuracy requirement of scanning microscopy, hinder the wide application of miniaturized systems. On the other hand, "in-flow" imaging involves continuous imaging of the cells that flow through the sensing area, thereby increasing the number of measured cells. Nevertheless, the flowing cells could be imaged with clear morphological features at low translocate velocity, while the motion blur will become an issue as cell velocity increases (Balsam et al., 2015). In this regard, "in-flow" imaging is usually supplemented with fluorescence staining, such as the identification of WBCs (Balsam et al., 2014; Zhu et al., 2011), MCF7 (Tan et al., 2014), and rare cells (Balsam et al., 2015). Moreover, a syringe pump is typically required as a sample-driven power source. These additional labeling and equipment increased operating costs and inconvenience for POCT. As a result, there is a high desire for a yet-to-be-developed, fully integrated label-free "in-flow" imaging microscope. There are mainly two challenges in realizing the miniaturization of the "in-flow" imaging microscope for the POCT of BCC. First, the cell velocity is restricted due to the limited image sensor frame rate (usually 30–60 frames per second, fps). This could lead to cell sedimentation and deposition in the inlet (cavity, tube, and reservoir). The concentration of cells that flow through the imaging area

is inconsistent with that of the original sample. Second, the liquid flow in the microchannel is laminar due to the low Reynolds number, which leads to a parabolic velocity field. Non-spherical cells (RBCs) rotate randomly under asymmetric shear force (Gu et al., 2014; Jagannadh et al., 2015; Yaginuma et al., 2012) and the morphological images at some special tilt angles are similar to those of other subpopulations in some extent. The traditional recognition method based on a single-frame morphological image could hardly be accurate.

In this paper, we focused on these two challenges and explored a novel fully-integrated smartphone-based label-free POCT method and system of BCC, with enhanced recognition and counting precision by using single-cell rotation and multi-frame morphology analysis. The integrated system is assembled based on the principle of a single-lens microscope with a smartphone. A miniaturized magnetic stirring model is introduced to avoid the cell concentration variation over time caused by sedimentation. The rotation of RBCs is realized with a shrinkage-expansion structure, where the liquid velocity field is regulated to enlarge the asymmetry of shear force acting on the cells. The shrinkage-expansion region is also taken as the imaging area, and the cell motion trails are tracked with multi-angle morphology imaged. Eventually, the cells are recognized and classified based on multi-frame morphological images. Moreover, systematic simulation is carried out to validate the functional stability of microstructures at a wide range of flow rates (mean velocity of outlet $\overline{V_o} = 50, 100, 500, 1,000, 2000\ \mu m/s$). The temporal consistency of cell concentration is experimentally verified with whole blood diluted in $1 \times$ PBS at various ratios (1:30, 1:40, 1:50, 1:200). The results indicate that the throughput is approximately 8000 cells/min, and the limit time that cell concentration remains consistent is about 1 h. With the multi-frame analysis method, we improved the average precision (AP) of single-cell recognition from 0.8622 to 0.9934. As for the clinical applications, we validate this approach with samples and identified all the cell concentration abnormalities (RBC 18 cases, WBC 22 cases, PLT 35 cases). A good agreement ($R^2 > 0.98$) was observed between our POCT device and the commercial clinical equipment, validating the potential application of our device for diagnosing abnormal blood cell morphology or concentration in the field setting.

2. Materials and methods

2.1. Microfluidic chip fabrication

The microfluidic chip consists of a sample reservoir, a microchannel, a waste reservoir, and a metallic capillary. The sample reservoir was made of polymethyl methacrylate (PMMA) with a capacity of 300 μL. The microchannel and waste reservoir were made of polydimethylsiloxane (PDMS) by casting onto the SU8 casting mold. It consists of two layers with different thicknesses: the microchannel with ~20 μm, and the waste reservoir with 2 mm. The casting mold of the microchannel was fabricated by a standard lithography (SU8-2025, Microchem) process on a 4-in. Silicon wafer. The PDMS replica was permanently bonded to the cover glass (thickness ~ 0.5 mm) through oxygen plasma treatment. A pair of aligning marks were fabricated on both the PDMS replica and cover glass to ensure that the imaging region is in the center of the chip. The sample reservoir was assembled into the inlet of the PDMS replica, and the metallic capillary was inserted into the waste reservoir. After fabrication and assembly, the microfluidic chip was sealed with 1% BSA (Thermo Scientific™) for 30 min to avoid non-specific adsorption.

2.2. Blood samples

This study was approved by the Institutional Ethical Review Board of the First Affiliated Hospital of Zhengzhou University (Zhengzhou, China). All methods were performed following ethical guidelines and

regulations. 85 peripheral whole blood samples were collected from patients with abnormal concentrations of RBC, WBC, and PLT, and 5 samples were provided by healthy donors undergoing physical examination in the First Affiliated Hospital of Zhengzhou University. For the validation of cell concentration temporal stability, 10 μL of healthy blood was diluted in 290 μL, 390 μL, 490 μL, and 1990 μL 1 × PBS, to prepare blood cell suspension with dilution rates (blood: PBS) of 30-fold, 40-fold, 50-fold, and 200-fold, respectively. As for the analysis of patient blood samples, 3 μL of blood was transferred into the sample reservoir through a well-designed capillary, where 147 μL of 1 × PBS and a micro stirring bar were pre-loaded.

2.3. Testing protocol

The 3 μL of finger-prick blood was collected using a homemade capillary tube and transferred into the sample reservoir. The quantitative tube is integrated with a 20 μL disposable glass capillary tube and a 0.2 mL disposable plastic transfer pipette. The inner diameter of the capillary tube is about 0.68 mm. Therefore, 3 μL of a blood sample could be quantitatively collected due to capillary force with the tube cut to a fixed length of 8.3 mm. After the sample is collected, plug the reserved opening with the fingers and press the top of the plastic transfer pipette, the blood could be transferred into the sample reservoir, where 147 μL of 1 × PBS and a micro stirring bar were pre-loaded. The microfluidic chip was inserted into the IOM and then pushed along the guideway into the analyzer. The IOM could be locked by the spring clasp and remain stable. The smartphone was set on the analyzer with the imaging camera aligned with the imaging area on the chip. The IMO could be released by pushing it again when the testing was finished. Finally, the cells are recognized and classified based on the YOLO-V4 model.

2.4. YOLO-V4 model related data sets and morphology analysis

A neural network of YOLO-V4 was used to make a preliminary evaluation of the separability of the images and the actual decision of the cell types (WBC, RBC, PLT), respectively. About 2900 RBC images, 2350 WBCs images, and 2350 PLTs images were collected and divided as the training set, the validation set, and the test set. The total set contains 4000 training images (2000 RBCs, 1000 WBCs, and 1000 PLTs), 1100 validation images (400 RBCs, 350 WBCs, and 350 PLTs), and 2500 test

images (500 RBCs, 1000 WBCs, and 1000 PLTs, more specifically, the ground truth of these 3 types of cells in the test set images were 1,000, 1,000, and 1,000, respectively). (See Supplementary for detailed information).

3. Results and discussion

3.1. Working principle

The working principle of the label-free "in-flow" imaging microscope is shown in Fig. 1A. The system is mainly integrated based on the single-lens microscopy imaging principle. The schematic of the smartphone-based single-lens microscope is shown in Fig. S1, with the optical magnification $k = f_1/f_0 \approx 45.45$. A microfluidic chip is used to regulate the spatial distribution and flow patterns of single cells (Fig. 1B). The initial 3D random distribution (Fig. 1B (i)) of blood cells could be single-layer arranged (Fig. 1B (ii)) by limiting the height of the microchannel to be similar to the cell size. And then, the cells are arranged in a straight-line pattern (Fig. 1B (iii)), to reduce aggregation and interaction with adjacent cells in the rotation region. A series of morphological images are captured as a single-cell flows through the imaging region with rotation (Fig. 1B (iv)). After that, the images are uploaded and the motion trajectories (Fig. 1C (i)) of single cells are tracked, as well as the morphological images (Fig. 1C (ii)) of successive frames. The single cell could be imaged at various angles while rotating, and the multi-angle morphological images are used for subpopulation recognition. Finally, the identification results are counted (Fig. 1C (iii)) and the statistical results are returned. The misidentification will be markedly decreased in comparison to the traditional single-frame or "stationary" identification method. In the end, the statistic counting results are obtained with improved accuracy.

3.2. Microfluidic chip design and instrumentation

In this work, the microfluidic chip was assembled with a sample reservoir, a waste reservoir, and a metallic capillary (Fig. 2A). The chip was designed with two major functions: cell arrangement in line-pattern and rotation. An interlaced pinching structure was applied to implement a line-patterned arrangement, making the cells pinched in succession by the protruding blocks at the top and bottom. And the rotation was
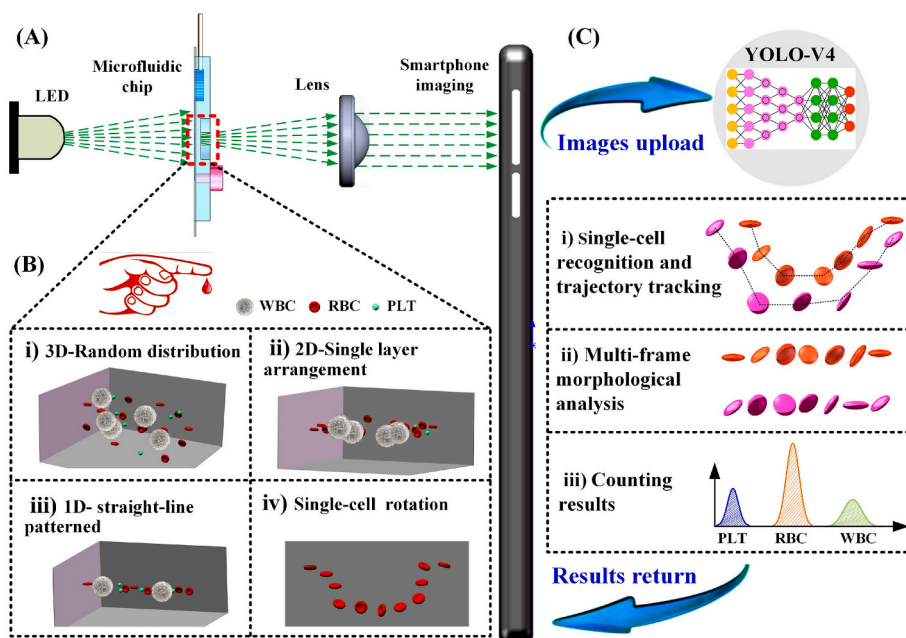

Fig. 1. (A) The principle of smartphone-based "in-flow" imaging for an improved blood cell count. (B) Schematic of cells manipulation process. (i) Cells in the initial state are randomly distributed in 3 dimensions; (ii) Cells are focused into a plane with limited height; (iii) Cells are arranged in a straight-line pattern; (iv) Single-cell flows through with rotation. This region is also taken as an imaging area to capture a series of morphological images. (C) Detection flow of multi-frame analysis of a single-cell. The images are uploaded and analyzed, and then the results are returned to the smartphone. (i) Trajectory tracking of a single-cell; (ii) Multi-frame analysis for reducing false identification; (iii) Count and perform statical analysis.
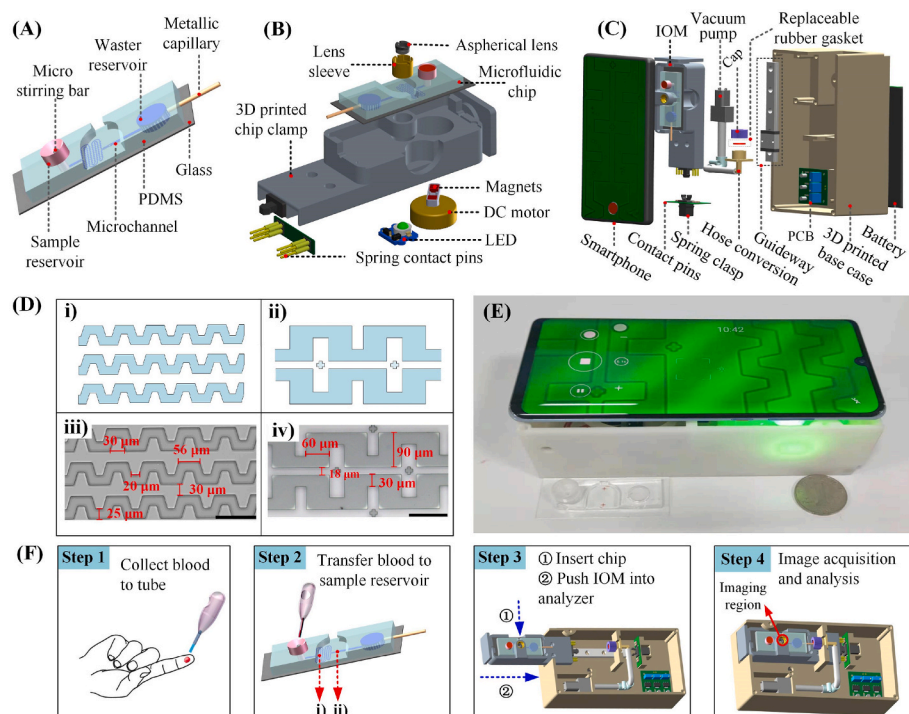
Fig. 2. (**A**) Structure chart of the integrated microfluidic chip. The chip consists of a sample reservoir, a microchannel, a waste reservoir, and a metallic capillary. (**B**) Exploded view of the IOM. (**C**) Exploded view of the fully integrated POCT device of BCC. (**D**) i) - ii) Schematic of an interlaced pinching structure for line-patterned arrangement and shrinkage-expansion structure for the rotation. iii) Microscopic of the interlaced pinching structure. A total length of 5 cm was used to handle high-cell-concentration samples. iv) Microscopic of shrinkage-expansion structure. The dimensions of the shrinkage area are 40 μm (length) × 30 μm (width), and these of expansion area is 60 μm (width) × 90 μm (length). The scale bar is 100 μm. (**E**) Image of a microfluidic chip and the "in-flow" imaging POCT device. The footprint is $15.5 \times 8 \times 5$ cm^3. (**F**) Overall workflow. Step 1: Collect blood in a tube. Step 2: Transfer the collected blood to the sample reservoir on the chip. Step 3: Insert the chip into IOM and push IOM into the analyzer. Step 4: Align the smartphone camera with sing-lens and record the videos of the cell flow.

realized with a shrinkage-expansion structure. A pair of symmetric shrinkage-expansion structures were used to increase analysis throughput.

The fully integrated portable platform was designed in SolidWorks and prototyped by a 3D printer. The device has a small footprint of 15.5 × 8 × 5 cm^3 and consists of optical, electromechanical, and image subsystems. A detailed bill of material to replicate our device is listed in Supplementary Table S1.

3.2.1. Optical subsystem

Based on the single-lens microscopy imaging principle, the optical subsystem was assembled with an aspherical lens (C392TME-A, $f_0 = 2.75$ mm, Thorlabs), a LED ($\lambda = 510$–530 nm, divergence angle = 120°, Jlotu) light source, and a smartphone (P30 pro, $f_1 = 125$ mm, Huawei). There is a relatively obvious difference between cells and water in the absorbance at the green spectral waveband, and the green light has the highest transmittance with the Bayer filter of RGGB array architecture. Therefore, we used the green LED to acquire images with high contrast and spatial resolution. The LED and aspherical lens were mounted on a 3D printed chip clamp, to maintain the distances between the LED, aspherical lens, and microfluidic chip constant. Especially, the lens was equipped with a lens sleeve for longitudinal position adjustment. The assembled optical subsystem was termed the integrated optical module (IOM) (Fig. 2B).

3.2.2. Electromechanical subsystem

The entire system was powered by a rechargeable 3.3 V portable Lithium-ion battery and could last for >30 h before recharging. Three customized printed circuit boards (PCBs) with multi-voltage converters were used for driving the micro vacuum pump, the magnetic stirring DC motor, and the LED. The DC motor aligned with the center of the sample reservoir was embedded in the IOM and electrically connected by the spring contact pins. The micro-stirring bar pre-loaded in the sample reservoir moves in a circle with the rotation of the magnets assembled on the DC motor (Fig. 2B). Finally, the IOM was integrated with a guideway and housed inside a 3D-printed base case. As for the sample driving, the vacuum pump was connected to a housed conversion, which was sealed

by a replaceable headspace crimp cap and PTFE septa. The sub-atmospheric pressure could be regulated by adjusting the supply voltage of the vacuum pump, to verify the cell flow velocity. The IMO could be pushed into the base case along the guideway, and be locked with the spring clap. Meanwhile, the septa could be pricked by the metallic capillary of the microfluidic chip, and then the LED, magnetic stirrer, and pump were powered.

3.2.3. Image subsystem

The microfluidic chip can be observed by the assembled optical subsystem IOM. The microscopic images were acquired by the smartphone at 30 fps and transformed to grayscale. The gray image was preprocessed by a built-in algorithm with background noise removed and contrast-enhanced. A custom-built program was developed to track the trajectory of a single cell when it flowed through the imaging region. Meanwhile, the multi-angle morphology of single-cell in the multi-frame images was collected for recognition with YOLO-V4.

The fully integrated POCT device of BCC was shown in Fig. 2C. The diagrams and microscopics of cell arrangement in line-pattern and rotation are listed in Fig. 2D (i - iv). Finally, the chip was fabricated and assembled into the fully integrated analyzer (Fig. 2E). And the four steps of the workflow are illustrated in Fig. 2F. With the integrated device and single-use microfluidic chip, the material cost is about 0.857 $/test (Supplementary Table S2).

3.3. Simulation of cell rotation structures

As is well known, it is very difficult to integrate complex and sophisticated sample pump systems into a portable device. We should make sure the microchannel structure designs of the microfluidic chip maintain stability, even if the pump pressure varies dramatically. We conducted a systematic simulation with COMSOL Multiphysics 5.6, to evaluate the stability and robustness. The flow field of laminar flow in the microchannel is axisymmetric, therefore, we simplified the simulation with a 2D model. The average liquid velocity at the outlet $\overline{V_o}$ was used to represent the flow rate. The non-spherical RBCs were modeled as rectangles (2 μm × 8 μm). (See Supplementary and Fig. S2 for the key

parameters of the simulation).

Assuming that, RBCs are randomly distributed on the sample plane in the spacious open area, where the width is 60 μm. A cell-arrangement microchannel with a total length of 500 μm was involved in the simulation. Simulations were carried out at different flow rates, $\overline{V_o} = 50, 100, 500, 1,000, 2000$ μm/s respectively. Fig. 3A shows the steady state of velocity field distribution and the arrangement results when $\overline{V_o}$ is 50 and 2000 μm/s (See Supplementary Fig. S3 and Movie 1

Supplementary data related to this article can be found online at https://doi.org/10.1016/j.bios.2022.115012

For complete simulation results at different flow rates). It is clear that, as the laminar flow was alternately regulated, cells in liquid were gradually transferred to the central axis of the microchannel. Moreover, compared to the initial 2D distribution, the distance between line-patterned cells was enlarged due to the velocity difference induced by the positional deviation. As illustrated, the first RBC reached the outlet at 11.3 s and the distance between the first and last RBCs was about 316 μm when $\overline{V_o}$ was 50 μm/s, while the distance was enlarged to 319 μm at 0.294 s when $\overline{V_o}$ was 2000 μm/s.

As for the cell rotation, We designed the microstructure mainly based on two factors: 1) Try to make the best use of the area in the field of view, to increase the detection throughput; 2) To meet the demand that the velocity of the POCT system could hardly remain stable, a simple structure is needed to achieve stable performance. We analyzed the influence of the width ratios between shrinkage/expansion regions and the radius of corner chamfers on laminar flow distribution (See Supplementary and Fig. S4 for detailed information). And then, we analyzed the steady state of velocity field distribution (Fig. 3B), the flow trajectories and rotation postures of single-cell (Fig. 3C and D), and the consistency of trajectories (Fig. 3E) (See Supplementary Fig. S5 and Movie 2.

Supplementary data related to this article can be found online at https://doi.org/10.1016/j.bios.2022.115012

For complete simulation results at different flow rates and initial positions). The single-cell rotation was realized using a shrinkage-expansion structure in this work (Fig. 3B). We set single cells with

different pose positions and orientations at the entrance of the shrinkage-expansion structure and analyzed the rotation angles while cells flowed through. Three RBCs are positioned at the upper, middle, and lower of the entrance with tile angles of 45°, 0°, and 315°, respectively. With the flow rate varying from 50 to 2000 μm/s, the normalized flow field maintains much the same, resulting in the rotation of all the RBCs (Fig. 3C and D). Moreover, the rotation patterns are much different due to the asymmetric shear forces resulting from the absolute value of velocity contrast, the rotations of upper and lower RBCs are much more drastic than those of the middle RBCs. On the other hand, the centroids of cell trajectories were manually tracked (Fig. 3E). As illustrated, due to the constant flow field distribution, RBCs with the same pose positions and orientations followed the defined trajectories at different flow rates (50, 100, 500, 1,000, 2000 μm/s). The consistency and certainty of motion trajectories indicated the feasibility of cell tracking in the following processing, even using high cell concentration samples.

3.4. Single-cell rotation and trajectory tracking

Based on the above analysis and simulation, experiments using healthy blood samples for evaluating single-cell rotation and trajectory tracking were carried out. The whole blood sample was diluted in $1 \times$ PBS with a dilution rate of 50-fold.

Fig. 4A shows a single frame of the videos recorded by a smartphone. The FOV is approximately 487.5×225.5 μm^2, and the physical size of the imaged object corresponding to a single pixel is about 0.21×0.21 μm^2. An area that contained a shrinkage-expansion structure was selected as identify region for cell trajectory tracking and multi-frame morphology imaging. We first analyzed the motion trajectories of a mass of single cells that flowed through within 20 min to evaluate the definiteness of single-cell trajectories, and the scattering plot of cell locations was drawn (Fig. 4B). As illustrated, cells are most likely to appear at the intermediate locations, where the flow rate is relatively high. Particularly, the scattering plot is consistent with the steady-state simulation result of velocity field distribution in Fig. 3B, which means that cells transfer through the imaging area in laminar flow and the
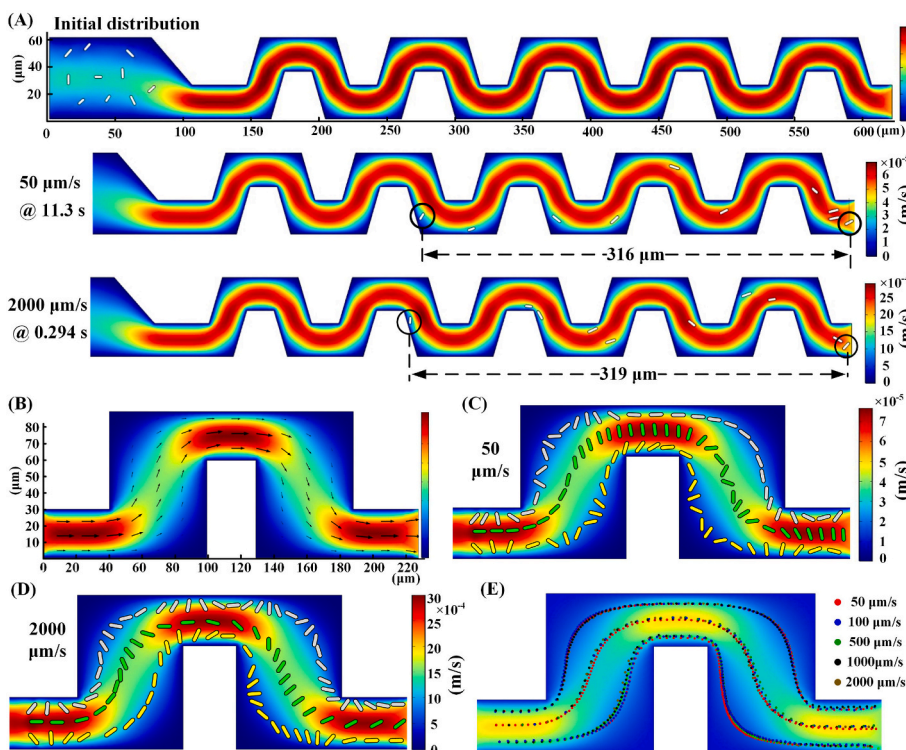

Fig. 3. Simulation results of straight-line pattern arrangement and rotation structures. (**A**) Steady-state velocity field distribution and the straight-line pattern arrangement results when $\overline{V_o}$ is 50 and 2000 μm/s. (**B**) The steady state of velocity field distribution of the shrinkage-expansion structure. (**C**)–(**D**) The trajectory and rotation pose of RBCs entering the microstructure from different positions at different tilt angles. The tile angles of the upper, middle, and lower RBCs are 45°, 0°, and 315°, respectively. The $\overline{V_o}$ in (**C**) is 50 μm/s and 2000 μm/s in (**D**). (**E**) The trajectory synthesis results when $\overline{V_o}$ is 50, 100, 500, 1,000, and 2000 μm/s, respectively. The initial positions and tilt angles of RBCs are the same as (**C**) and (**D**).
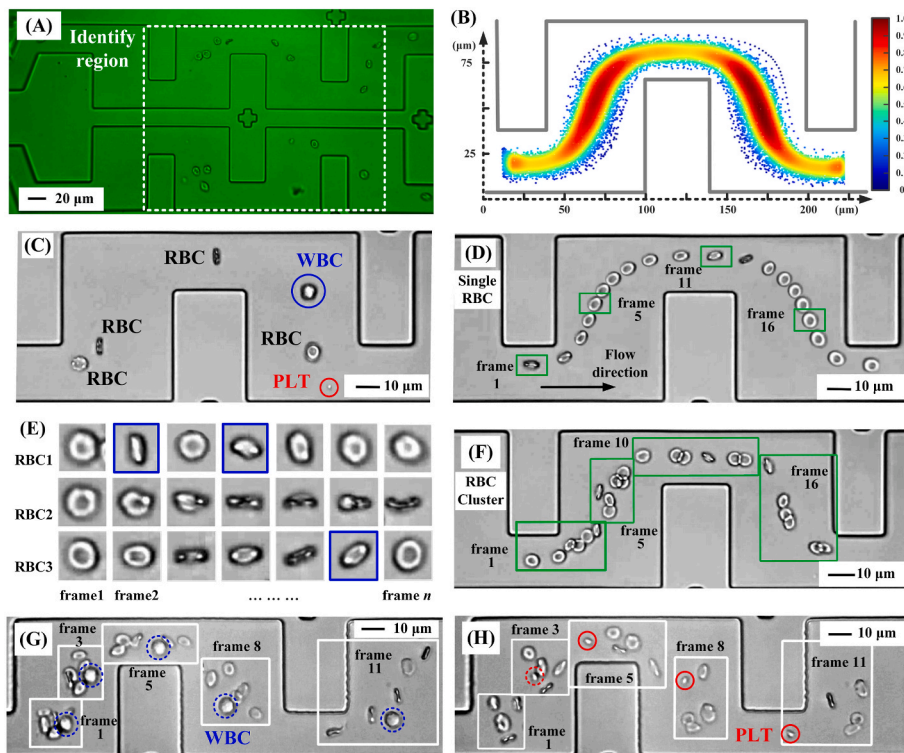
Fig. 4. (**A**) A single frame of the videos recorded by a smartphone. The FOV is approximately 487.5 × 225.5 μm². The scale bar is 20 μm. The region in the white dashed box is selected as identify region. (**B**) A scattered plot of locations that a mass of single cells flowed through within 20 min. (**C**) Typical morphological images of the WBC (blue circle), PLT (red circle), and RBCs (the rest cells). (**D**) The complete trajectory and multi-angle morphology of a single RBC at a low flow rate. Images (frames 1, 5, 11, and 16) with distinct morphological differences are marked with green squares. (**E**) 3 examples of typical RBC rotation image sequences. The images marked with blue squares are more likely to be identified as WBCs. (**F**) The trajectory tracking and identification of an RBC cluster with discontinuous frames. (**G**) The trajectory tracking and identification of an RBC cluster including one WBC with discontinuous frames. (**H**) The trajectory tracking and identification of an RBC cluster including one PLT with discontinuous frames. The scale bar in (**C**), and (**D–H**) is 10 μm.

trajectories are definite. Moreover, the single cell could be accurately tracked according to the location, even if the sequence of adjacent cells has changed.

The typical morphological images of the blood cell subpopulation were shown in Fig. 4C. The WBC (circled in blue) appears to be solid and highlighted with irregular dark boundaries. The PLT (circled in red) exhibits a sphere of a smaller size. Meanwhile, the gray values of PLTs are related to the longitudinal position in the microchannel. The RBCs (not circled) show visible morphology changes when rotating in the channel flow, including double circular rings, dumbbells, and other irregular forms. Furthermore, the complete trajectory of a single cell was illustrated, as well as the multi-angle morphology (Fig. 4D). With analysis of numbers rotation images of RBCs, various morphologies could be acquired (See Supplementary Movie 3.

Supplementary data related to this article can be found online at https://doi.org/10.1016/j.bios.2022.115012

Fig. 4E shows 3 examples of typical RBC rotation image sequences. It is clear that the morphologies of RBCs are much more complex and different, meaning that it is difficult to identify the cell as an RBC or a WBC when it is orientated at some special degrees, such as in the images marked with blue squares. Based on the analysis of RBC morphology, we found that the double-circular-ring pattern is the most representative feature of RBCs and could be used as the criteria for identification.

Except for the situation of single-cell transporting, there is still the opportunity that multi-cells to pass through together as a cluster (the RBC cluster, WBCs included in the RBC cluster, and PLTs included in the RBC cluster) (Fig. 4F–H and Supplementary Movie 4.

Supplementary data related to this article can be found online at https://doi.org/10.1016/j.bios.2022.115012

Due to the trajectory deviation caused by interaction between adjacent cells and the morphological change introduced by rotation, it is difficult to track every single cell within a cluster. Worse still, the probability of cell cluster occurrence and the overlap rate of cells increases with the decrease in dilution ratio for blood samples. In this work, we mainly took the cell cluster as one unit and the RBCs as background cells. The number of cells within the cell cluster could be

easily counted, and then, we just need to verify the existence or number of WBCs and PLTs within the cluster. Fig. 4F shows an example of the RBC cluster, just as the 4 frames illustrated, there are 6 target cells in the RBC cluster, and no "suspected WBCs or PLTs" appear in the consecutive frames. Therefore, we could exclude the presence of WBCs or PLTs and identify all cells as RBCs. On the other hand, the WBC is approximately spherical, while the PLT is relatively small, and the morphologies of WBC and PLT remain stable when flowing through the microchannel. As for the example of one WBC included within the cell cluster (Fig. 4G), the cells are heavily overlapped in frames 1 and 3, and the number and type cannot be identified. However, with the cluster flowing through, the distances between the cells are enlarged. Meanwhile, there is one "suspected WBC" in each frame (frames 1, 3, 5, 8, 11). Therefore, the cell cluster could be identified as 1 WBC and 5 RBCs. Similarly, the cell cluster includes one PLT (Fig. 4H) could be easily distinguished as 1 PLT and 4 RBCs, even though the PLT is missing in frame 1 resulting from cell overlap. In summary, the cell posture and relative position varied due to cell cluster flow, and the overlap between multiple cells could be effectively improved, and the accuracy of identification and counting is enhanced in turn.

We checked all the videos acquired with blood samples at different dilution ratios and found that the clusters are incidental, even for the RBCs (the highest subclass content). In our opinion, the effective suppression of cell clusters mainly benefited from our whole in-flow process, especially the appropriate dilution and well-designed single-cell arrangement structure equipped with a micro-magnetic stirring.

3.5. Performance evaluation with the healthy sample

After validating all of the subsystems and system integration, we tested the performance of the "in-flow" imaging analyzer. The performance of the cell recognition and counting algorithm, the effectiveness of the multi-frame analysis method, and the cell concentration temporal stability were evaluated respectively. Here, healthy blood samples were used.

3.5.1. Cell recognition and counting

The learning history from the model training during iterations is shown in Fig. 5A. As illustrated, when the training iterations reach about 10,000 iterations, the final loss value is stable at approximately 0.55 and the final mean Average Precision (mAP) value of the validation set reaches 98.48%, which indicates that the training converges as expected and works well. The statistical confusion matrix of the test set is shown in Fig. 5B. There are 12 RBCs misrecognized as WBCs, and 9 WBCs misrecognized as RBCs. Moreover, 0.3% of RBCs and 1.6% of PLTs are missed due to the overlap or agglomeration of adjacent cells. Fig. 5C shows the Precision-Recall (PR) curves of the test set. The average precision (APs) of all three types of cells reach 0.9819 or higher, which indicates a very high detection accuracy. (See Supplementary for detailed information).

3.5.2. Multi-frame analysis

To quantitatively compare the single-frame-based detection and multi-frame analysis method in terms of recognition effect, here we took WBCs as an example and analyzed the consecutive 5 frame images of 500 WBCs. The WBCs are tracked with the algorithm we propose before (Du et al., 2022).

For single-frame analysis, one of the 5 consecutive frames of every single cell (500 WBCs and 500 RBCs) is selected randomly as single-frame images. We calculated the AP values of the 1000 random images, and plotted the statistical distribution (violin plot) on the left side of Fig. 5D. As shown, the AP values range from 0.7837 to 0.9807 with a mean value (Mean) of 0.8622 and a standard deviation (σ) of 0.0449.

The interval of numerical dispersion (Mean $\pm$ σ, 0.8173–0.9071) is marked with blue dotted lines.

With the multi-frame analysis method, the number of frames that a cell was identified as WBC was recorded as n ($1 \leq n \leq 5$). N values were used as the threshold to make a secondary classification decision on the target cells. Based on the obtained detection results, we calculated these corresponding AP values, as shown (red dots) on the right side of Fig. 5D. The AP of multi-frame analysis is significantly improved when n = 2, 3, 4, 5, and reaches the highest value of 0.9934 when n = 3. As illustrated in Fig. 5D, the misidentification caused by RBC rotation is greatly reduced, while n values increased from 1 to 3, resulting in increasing AP values. However, as the n value increases, the cells are not allowed to be missed at each frame, which is reflected in the decline of recall and AP values. Therefore, the AP values appear to earlier increase and later decrease trend.

3.5.3. Cell concentration temporal stability

During the cell flow testing, limited by the flow rate, cell sedimentation and deposition in the inlet would cause the concentration inconsistent between the tested sample and the original sample. We integrated a mini magnetic stirring structure in the IOM, to disturb the monodisperse cell in the reservoir to prevent cell sedimentation. The length of the stirrer is about 5 mm, and the rotation speed is 30 rpm. Healthy blood samples with different dilution rates of 200-fold, 50-fold, 40-fold, and 30-fold were tested. Fig. 5E shows the detected number of RBCs within 20 min. As illustrated, there is a good linear relationship between RBC counts and the test duration. Meanwhile, a lower dilution
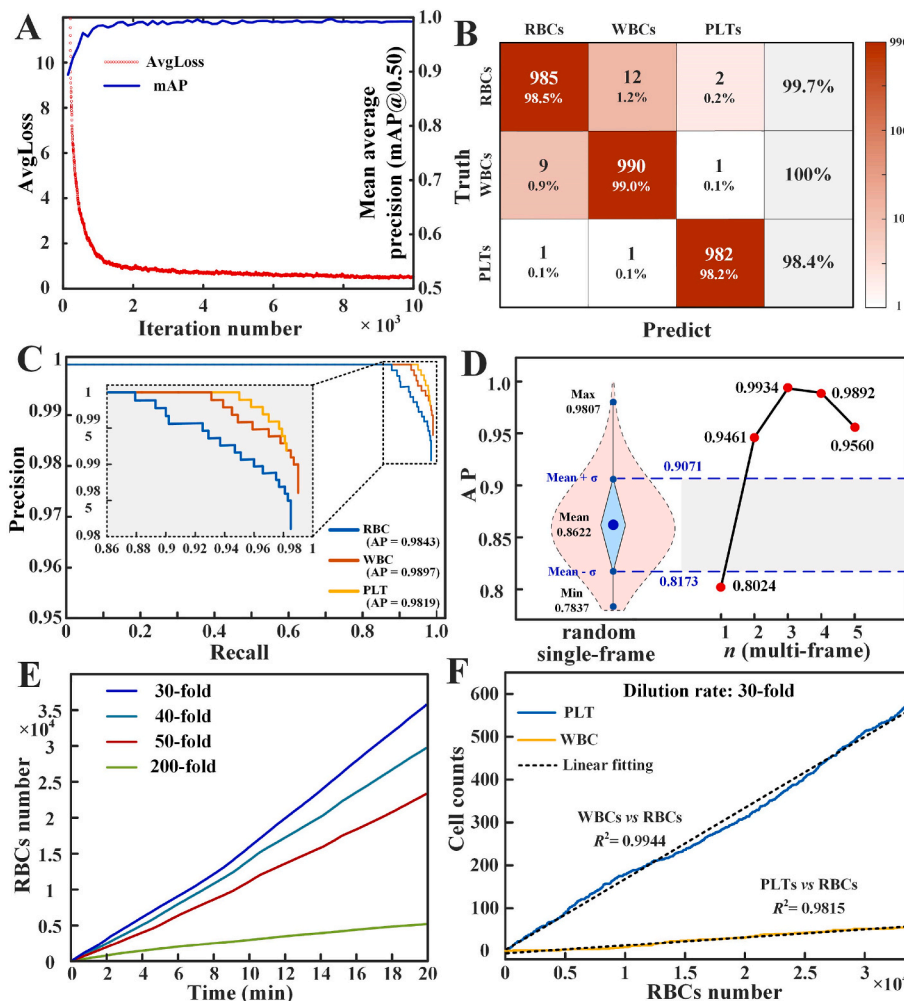

Fig. 5. (A) Training and validation process of the YOLO-V4 model. When the training iterations reached about 10,000 iterations, the model gradually saturated with a stable AvgLoss value of 0.55 and a mAP value of 98.48%. **(B)** Confusion matrix of the test set. The false identification of RBCs, WBCs, and PLTs is 1.4%, 1.0%, and 0.2% respectively. And the probability of RBCs and PLTs loss is 0.3% and 1.6%. **(C)** PR curves of the test set. The area under the PR curve is AP, which represents the average detection accuracy. **(D)** AP distribution of WBC identification with random single-frame and multiple-frame methods. The violin plot is the distribution of the single-frame analysis method, where, the AP value mainly ranges from 0.8173 to 0.9071 (**Mean $\pm$ σ**). With multi-frame analysis, the AP (red dots) is significantly improved and reaches the largest value of 0.9934 when n = 3. **(E)** The RBC counts within 20 min at a different dilution rate of 30-fold, 40-fold, 50-fold, and 200-fold, respectively. **(E)** The cell counts ratios between PLTs, WBCs, and RBCs at a dilution rate of 30-fold within 20 min. The coefficients (PLT *vs* RBC, 0.9944; WBC *vs* RBC, 0.9815) indicate good temporal stability of cell concentrations.

rate indicates higher throughput and a higher probability of cell overlapping and clustering. Finally, we found that a sample diluted at 30-fold with a throughput of about 8000 cells/min is the limitation that could be handled, and the limit time that cell concentration remains consistent is about 1 h. After that, the relative proportionality relation between WBCs, PLTs, and RBCs are analyzed (Fig. 5F). The coefficients (WBCs vs RBCs, 0.9815; PLTs vs RBCs, 0.9944) indicate a good agreement between the cell concentrations of each subclass.

3.6. Clinical blood sample test

Based on the above analysis and performance evaluation, we tested clinical samples to best evaluate the performance of the "in-flow imaging" analyzer. For the special touch, to avoid the detection error caused by the inaccurate liquid volume quantification, we characterized the cell concentration with count ratios ($R_{R/W}$, $R_{P/W}$) between cell subclasses, rather than the number of cells within the unit volume of liquid. Here, $R_{R/W}$ is the ratio between RBC count and WBC count, and $R_{R/W}$ is the ratio between PLT count and WBC count. For the same reason, in this work, we just analyzed the abnormal concentration of a single subclass. The BCC assay performed the initial diagnosis with commercial benchtop device LH750 (Beckman Coulter, USA) as the reference method to benchmark our analyzer. All the clinical blood samples were tested with dilution rates of 50-fold.

Firstly, 10 clinical samples (No: S_1 - S_{10}) were tested in the double-

blind trial, and the results of both analyzers are shown in Fig. 6A. Fig. 6B shows the relative errors ($E_{R/W}$, $E_{P/W}$) between the "in-flow imaging" analyzer and LH750, where, $E_{R/W} = \frac{R_{R/W}(in\_flow)-R_{R/W}(LH750)}{R_{R/W}(LH750)} \times$ 100%; $E_{P/W} = \frac{R_{P/W}(in\_flow)-R_{P/W}(LH750)}{R_{P/W}(LH750)} \times 100\%$. The results of "in-flow" imaging agree well with these of LH750, even if $R_{R/W}$ (LH750) ranges from 207.55 to 1273.63 and $R_{P/W}$ (LH750) varies from 1.99 to 56.72. Most of the relative errors $E_{R/W}$ and $E_{P/W}$ distribute in the region of (−10%, 10%). The detailed values of $R_{R/W}$, $R_{P/W}$, $E_{R/W}$, and $E_{P/W}$ are listed in Table S3. Based on the above results, we could conclude that the relative concentration ratio between RBC, PLT, and WBC in a wide fluctuating region could be detected accurately.

And then, to further evaluate the diagnostic sensitivity and specificity of the device, a scaled-up test of 75 clinical samples (RBC concentration abnormity, 18 cases; WBC concentration abnormity, 22 cases; PLT concentration abnormity, 35 cases) is carried out. The concentration abnormal of RBC and WBC could be characterized by $R_{R/W}$ in a union, therefore, the results of 40 cases test including RBC and WBC abnormity are drawn indiscriminately in Fig. 6C. The $R_{R/W}$ of "in-flow" imaging varies from 113.68 to 3007.94. A degree of fitting ($R^2 = 0.9848$) indicates a good agreement between the "in-flow" imaging device and clinical methods. The results of PLT concentration abnormity are shown in Fig. 6D. $R_{P/W}$ of "in-flow" imaging ranges from 1.70 to 244.98 with a coefficient of 0.9912 compared to LH750. Finally, the detection errors were statistically analyzed and shown in form of violin
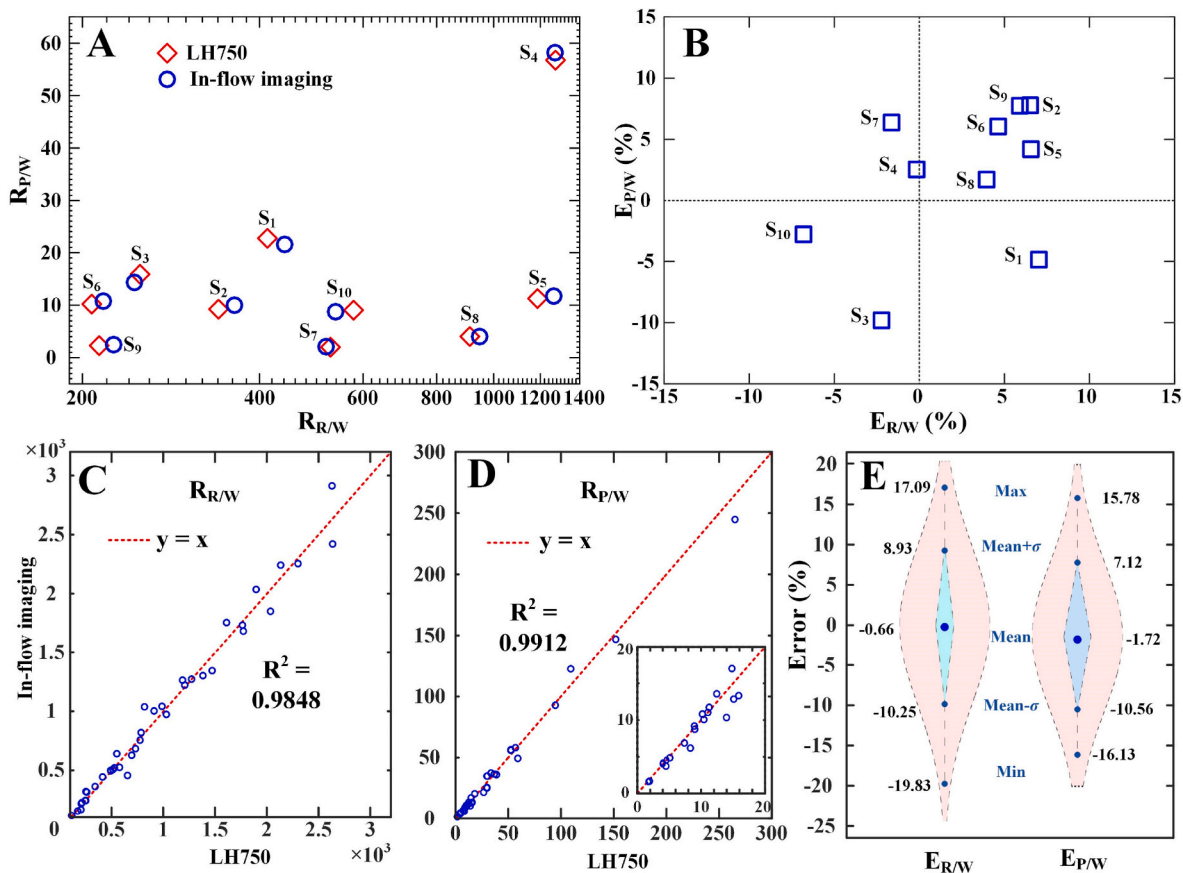

Fig. 6. The results of clinical samples. The cell concentration is characterized by count ratios ($R_{R/W}$, $R_{P/W}$) between cell subclasses. (**A**) The results of 10 samples in the double-blind trial. $R_{R/W}$ ranges from 207.55 to 1273.63, and the axis is plotted in logarithmic form. The results of "in-flow" imaging are close to these of LH750, and the relative errors ($E_{R/W}$, $E_{P/W}$) are scatted in (**B**). All the errors distribute in the region of (−10%, 10%), indicating a good agreement between "in-flow" imaging and LH750. The detailed data of (**A**) and (**B**) are listed in Table S3. (**C**) The comparison results of $R_{R/W}$ with the "in-flow" imaging method and LH750. Totally, 40 cases of patient samples with RBC or WBC concentration abnormal are tested. The degree of fitting is 0.9848. (**D**) The comparison results of $R_{P/W}$ with the "in-flow" imaging method and LH750. Finally, 35 cases of patient samples with PLT concentration abnormal are tested with a degree of fitting of 0.9912. The results where $R_{P/W} < 20$ are enlarged in the embedded box. The error distribution of $E_{R/W}$ and $E_{P/W}$ are shown in (**E**) with violin plots. The small **Mean** values (−0.66, −1.72) and standard deviations (9.59%, 8.84%) certify the sensitivity and specificity of the "in-flow" imaging method.

plots in Fig. 6E. The $E_{R/W}$ ranges from −19.83% to 17.09% with a mean value of −0.66%, and a standard deviation σ 9.59%. The $E_{P/W}$ ranges from −16.13% to 15.78% with a mean value of −1.72%, and a standard deviation σ 8.84%. Eventually, based on the results of LH750, the concentration abnormity of all samples is accurately identified with an "in-flow" imaging analyzer.

4. Conclusion

In summary, we demonstrated an "in-flow" imaging method with cell rotation and multi-frame analysis for improved identification and counting accuracy of BCC, and present a fully integrated POCT device. With the integration of mini magnetic stirring, we can handle whole blood samples at a dilution ratio of 30-fold for as long as 1 h with a throughput of about 8000 cells/min, without subclass cell concentration variation. Moreover, the misrecognition due to rotation during cell flow is effectively inhibited with multi-frame analysis. The AP value of WBCs identification is improved from 0.8622 to 0.9934. We have successfully demonstrated this concept by testing healthy and 75 cases of clinical whole blood samples with cell concentration abnormalities. The identification and count results agree well ($R_{R/W}$, $R^2 = 0.9848$; $R_{P/W}$, $R^2 = 0.9912$) with these of routine clinical BCC equipment LH750. With these efforts, we anticipate that the portable, easy-to-use device could enable individuals to perform highly accurate BCC testing at home.

Credit author statement

Wenchang Zhang: Designed and fabricated the microfluidic chips and POCT devices, Designed and performed the BCC experiment, Writing – original draft, Co-wrote the manuscript, With discussion from all authors. Ya Li: Designed and performed the BCC experiments, Co-wrote the manuscript, With discussion from all authors. Bing Chen: Designed and performed the BCC experiments, Co-wrote the manuscript, With discussion from all authors. Yuan Zhang: Collected the clinical samples and performed the initial clinical study. Ziqiang Du: Performed the identification algorithm. Feibin Xiang: Fabricated the microfluidic chips, With discussion from all authors. Yu Hu: Assembled the POCT devices, With discussion from all authors. Xiaochen Meng: Assembled the POCT devices, With discussion from all authors. Chunliang Shang: Designed and performed the BCC experiments, With discussion from all authors. Shengfa Liang: Performed the simulation, With discussion from all authors. Xiaonan Yang: Writing – original draft, Co-wrote the manuscript, With discussion from all authors. Weihua Guan: Conceptualization, and, Supervision, Writing – original draft, Co-wrote the manuscript, With discussion from all authors.

Declaration of competing interest

The authors declare that they have no known competing financial interests or personal relationships that could have appeared to influence the work reported in this paper.

Data availability

The authors do not have permission to share data.

Acknowledgments

Appendix A. Supplementary data

Supplementary data to this article can be found online at https://doi.org/10.1016/j.bios.2022.115012.

References

Balsam, J., Bruck, H.A., Rasooly, A., 2014. Analyst 139 (17), 4322–4329.
Balsam, J., Bruck, H.A., Rasooly, A., 2015. Biosens. Bioelectron. 64, 154–160.
Beck, N., 2009. Diagnostic Hematology. Springer.
Chen, L.F., Liu, Y.T., Xu, H.S., Ma, L.L., Wang, Y.F., Yu, L., Wang, F., Zhu, J.M., Hu, X.J., Yi, K.Z., Yang, Y., Shen, H., Zhou, F.L., Gao, X.Q., Cheng, Y.X., Bai, L., Duan, Y.W., Wang, F.B., Zhu, Y.M., 2021. Microsystems and Nanoengineering 7 (1).
Du, Z.Q., Li, Y., Chen, B., Wang, L.L., Hu, Y., Wang, X., Zhang, W.C., Yang, X.N., 2022. Lab Chip 22 (18), 3390–3401.
Go, T., Byeon, H., Lee, S.J., 2018. Biosens. Bioelectron. 103, 12–18.
Gu, Q.Y., Aoyama, T., Takaki, T., Ishii, I., 2014. Ieee Int Conf Robot 5848–5853.
Hernandez-Neuta, I., Neumann, F., Brightmeyer, J., Tis, T.B., Madaboosi, N., Wei, Q., Ozcan, A., Nilsson, M., 2019. J. Intern. Med. 285 (1), 19–39.
Ilyas, S., Sher, M., Du, E., Asghar, W., 2020. Biosens. Bioelectron. 165, 112417.
Jagannadh, V.K., Adhikari, J.V., Gorthi, S.S., 2015. Biomicrofluidics 9 (2).
Kanakasabapathy, M.K., Pandya, H.J., Draz, M.S., Chug, M.K., Sadasivam, M., Kumar, S., Etemad, B., Yogesh, V., Safavieh, M., Asghar, W., Li, J.Z., Tsibris, A.M., Kuritzkes, D. R., Shafiee, H., 2017. Lab Chip 17 (17), 2910–2919.
Kanakasabapathy, M.K., Thirumalaraju, P., Bormann, C.L., Kandula, H., Dimitriadis, I., Souter, I., Yogesh, V., Pavan, S.K.S., Yarravarapu, D., Gupta, R., Pooniwala, R., Shafiee, H., 2019. Lab Chip 19 (24), 4139–4145.
Kheireddine, S., Perumal, A.S., Smith, Z.J., Nicolau, D.V., Wachsmann-Hogiu, S., 2019. Lab Chip 19 (5), 825–836.
Lee, S.A., Yang, C., 2014. Lab Chip 14 (16), 3056–3063.
Meng, X., Huang, H.C., Yan, K.D., Tian, X.L., Yu, W., Cui, H.Y., Kong, Y., Xue, L., Liu, C., Wang, S.Y., 2016. Lab Chip 17 (1), 104–109.
Merazzo, K.J., Totoricaguena-Gorrino, J., Fernandez-Martin, E., del Campo, F.J., Baldrich, E., 2021. Diagnostics 11 (6).
Orth, A., Wilson, E.R., Thompson, J.G., Gibson, B.C., 2018. Sci Rep-Uk, vol. 8.
Rivenson, Y., Koydemir, H.C., Wang, H.D., Wei, Z.S., Ren, Z.S., Gunaydin, H., Zhang, Y. B., Gorocs, Z., Liang, K., Tseng, D., Ozcan, A., 2018. ACS Photonics 5 (6), 2354–2364.
Roy, M., Seo, D., Oh, S., Yang, J.W., Seo, S., 2017. Biosens. Bioelectron. 88, 130–143.
Ryan Zenhausern, A.S.D., 2022. Babak safavinia, seungmin han, paige E. Rudy, young-wook won, jeong-yeol yoon. Biosens. Bioelectron. 200.
Skandarajah, A., Reber, C.D., Switz, N.A., Fletcher, D.A., 2014. PLoS One 9 (5), e96906.
Smith, Z.J., Chu, K., Espenson, A.R., Rahimzadeh, M., Gryshuk, A., Molinaro, M., Dwyre, D.M., Lane, S., Matthews, D., Wachsmann-Hogiu, S., 2011. PLoS One 6 (3), e17150.
Tan, A.P., Dudani, J.S., Arshi, A., Lee, R.J., Tse, H.T., Gossett, D.R., Di Carlo, D., 2014. Lab Chip 14 (3), 522–531.
Walzik, M.P., Vollmar, V., Lachnit, T., Dietz, H., Haug, S., Bachmann, H., Fath, M., Aschenbrenner, D., Abolpour Mofrad, S., Friedrich, O., Gilbert, D.F., 2015. Biosens. Bioelectron. 64, 639–649.
Wang, Y.L., Chen, D.N., Guo, X.L., 2022. Biotechnol. Lett. 44, 1301–1311.
Wu, T.F., Mei, Z., Lo, Y.H., 2013. Sensor Actuat B-Chem 186, 327–332.
Yaginuma, T., Pereira, A.I., Rodrigues, P.J., Lima, R., Oliveira, M.S.N., Ishikawa, T., Yamaguchi, T., 2012. Computational vision and medical image processing, 2011 Vipimage 217–220.
Yang, K., Wu, J.D., Santos, S., Liu, Y., Zhu, L., Lin, F., 2019. Biosens. Bioelectron. 124, 150–160.
Zare Harofte, S., Soltani, M., Siavashy, S., Raahemifar, K., 2022. Small, e2203169.
Zhang, W.C., Hu, Y., Choi, G., Liang, S.F., Liu, M., Guan, W.H., 2019. Sensor Actuat B-Chem 296.
Zhu, H., Mavandadi, S., Coskun, A.F., Yaglidere, O., Ozcan, A., 2011. Anal. Chem. 83 (17), 6641–6647.
Zhu, H., Sencan, I., Wong, J., Dimitrov, S., Tseng, D., Nagashima, K., Ozcan, A., 2013. Lab Chip 13 (7), 1282–1288.